Multi-Fidelity Surrogate Model for Interactional Aerodynamics of a Multicopter

Orazio Pinti PhD Student
Assad Oberai Professor
Computation and Data Driven Discovery Group
University of Southern California
Los Angeles, CA

Richard Healy PhD Student
Robert Niemiec Research Scientist
Farhan Gandhi MOVE Director
Center for Mobility with Vertical Lift
Rensselaer Polytechnic Institute
Troy, NY

ABSTRACT

The growing interest in large electric multicopters (eVTOL aircraft) has prompted the search for methods that can accurately and efficiently predict their aerodynamic performance under different designs and operating conditions. The challenge is modeling the complex interactional effects of rotors operating in close proximity. This can be tackled with high-fidelity computational fluid dynamics (CFD) models, which capture the physics of rotor interaction from first principles. However, they are computationally demanding for performing studies over a range of parameters. On the other hand, lower-fidelity models are computationally inexpensive, but approximate the underlying physics and can be imprecise in predicting the fields of interest. In this study we present a multi-fidelity approach that inherits the accuracy of a high-fidelity model, while retaining most of the computational efficiency of a low-fidelity model. In this approach, the low-fidelity model is used to investigate the entire space of parameters and identify key parameter values to perform high-fidelity simulations. Thereafter, these high-fidelity simulations are used in a lifting procedure to determine multi-fidelity solutions at desired parameter values. We apply this strategy to determine the rotors' lift and drag distributions of a 2-rotor assembly in forward flight. The parameters considered are design variables, namely the longitudinal and vertical rotor-to-rotor separation, and operating conditions variables: forward speed and disk loading (DL). We conclude that over a large of parameters this approach yields results that retain the accuracy of the high-fidelity predictions at the computational cost of the low-fidelity model.

INTRODUCTION

The last decade has seen a surge of interest in large eVTOL aircraft for Urban Air Mobility, commercial package delivery, and military applications. With the current battery energy density limitations, it is especially important to maximize eVTOL aircraft aerodynamic performance. Therefore, a time-efficient aerodynamic characterization that accounts for the complex interaction between the rotors at various multicopter design and operation conditions becomes very appealing. While high-fidelity CFD models provide a detailed description of the physics of multi-rotor interaction, in most cases, they are too computationally demanding to perform studies over a range of parameters. In these cases, lower-fidelity models, with simplified physics or other approximations, are used instead. However, these lower-fidelity models typically incur larger errors in predicted quantities of interest (QoIs), such as thrust, torque, and power. It is therefore useful to develop multi-fidelity methods that combine the desirable characteristics of both high- and low-fidelity models. That is, they inherit the computational efficiency of the low-fidelity model, while retaining the accuracy of the high-fidelity model.

Multi-fidelity methods have a rich history of application in different areas of science and engineering. The reader is referred to Fernández-Godino et al. (Ref. 1) and Peherstofer et al. (Ref. 2) for two comprehensive reviews of these methods. In Peherstofer et al., the authors classify these methods into three categories: adaptation, fusion and filtering. Methods that fall in the adaptation category begin with a low-fidelity model and adapt it by adding terms that are driven by the results from the high-fidelity model. On the other hand, model fusion methods use predictions from low-fidelity and high-fidelity models in a third "fused" multi-fidelity model. Finally, methods based on the filtering approach use predictions from the low-fidelity model to determine the precise parameter values where high-fidelity predictions are to be performed, and then use these results either to adapt the low-fidelity model, or to fuse the low- and high-fidelity models. When viewed from this perspective, the multi-fidelity model developed in this study relies on fusion and filtering. In particular, it fuses a high- and a low-fidelity model into a another model. Further, it relies on filtering since it prescribes the points in the parameter space where the high-fidelity model ought to be deployed.

The multi-fidelity approach presented in this paper was developed in (Ref. 3), further analyzed in (Refs. 4,5), and applied to topology optimization under uncertainty in (Ref. 6). It comprises of the following steps:

1. Perform a large number of low-fidelity simulations to generate snapshots that span the domain of interest in the parameter space.

2. Identify the parameter values corresponding to the most

Presented at the Vertical Flight Society's 77th Annual Forum & Technology Display, Virtual, May 11–13, 2021.

important low-fidelity snapshots, and then express each of the remaining snapshots in the set in terms of these important snapshots.

3. Perform high-fidelity simulation at the parameter values corresponding to the important snapshots to generate their corresponding high-fidelity counterparts.

4. Use the expansion coefficients computed in Step 2, but with the high-fidelity snapshots computed in Step 3, in order to construct the multi-fidelity surrogate of the solution in the entire parametric domain of interest.

We note that several numerical methods can be employed to determine the important snapshots in Step 2 above (Ref. 7). These include leverage sampling, which is an singular-value-decomposition-based method to solve the column subset selection problem (CSSP) (Refs. 8, 9), a pivoted Cholesky decomposition (Refs. 3, 4), or a pivoted QR decomposition (Refs. 10–12). In this work we utilize the QR decomposition, since it is computationally efficient and robust (Refs. 13, 14).

We apply this multi-fidelity approach to predict the aerodynamic performance of a two-rotor system in forward flight, when both design variables and operating conditions are varied. The four parameters we consider are the longitudinal and vertical distance between the two rotors, d_x and d_y (Fig. 1), the forward speed V, and the disk loading DL. The fields we are interested in predicting are the lift and drag distribution for both rotors, from which the total rotors' thrust and torque can be computed. For the high-fidelity model we use a CFD model of the system and for the low-fidelity model we use the RMAC model (Ref. 15), which is based on a blade element approximation. In Ref. 16, we have applied this approach to investigate the effect of rotor-separation only. In this work we extend the study to include the effect of disk loading and forward speed.

The format of the remainder of this manuscript is as follows. In the following section we formulate the problem of interest by describing the high-fidelity and the low-fidelity models in detail and our strategy for combining them. Thereafter, we present numerical results, and end with conclusions.

PROBLEM FORMULATION

We analyze the aerodynamic behavior of the rotors of a two-rotors multicopter in forward flight, outlined in Fig. 1. The rotors are located in the longitudinal plane, aligned with the forward velocity, and the fields of interest are the disk plots of lift and drag. The relative position of the rotors can be described using the inter-rotor longitudinal and the vertical distance, denoted by d_x and d_y. Together with the operating conditions of forward speed V and disk loading DL, a four-dimensional parameter space $\boldsymbol{\theta} = (d_x, d_y, DL, V)$ for the system of interest is defined. At each point, $\boldsymbol{\theta}$ in the parameter space we can associate a value of the fields of interest, namely the lift and drag distribution. The two different fidelity models used to investigate the behavior of the dual-rotor multicopter are a high-fidelity CFD model, and the lower-fidelity blade element theory model.

High-Fidelity Model – CFD

CFD simulations are conducted using the commercial Navier-Stokes solver AcuSolve which uses a stabilized 2^{nd}-order upwind finite element method. AcuSolve simulation results for an SUI Endurance rotor in hover were previously shown to compare well against experiment in Ref. 17. For a two-rotor unit, the computational domain is shown in Fig. 2a, comprising of a rectangular prism with far-field boundary conditions on the front and top surfaces set to the freestream velocity. The sides, bottom and rear of the computational domain are set to outflow with backflow conditions enabled, which allows for flow in either direction across the boundary with zero pressure offset. All boundaries of the computational domain are at least 25 rotor radii away from the center of the 2-rotor assembly in all directions. As indicated in Fig. 2a, within the volume resides two cylindrical rotating volumes (one for each rotor), where the mesh inside the volume rotates along with the rotor geometry. Each rotating volume is a cylinder with radius $1.06R$. The height of the cylinder extends two tip chord lengths above and below the rotor plane. Each rotating volume is bounded by a sliding mesh interface which passes information into and out of the non-rotating volume that comprises the remainder of the computational domain.

The domain is discretized using a mesh comprised entirely of unstructured tetrahedral elements. Within both rotating volumes, the blade surface mesh is set to ensure 200 elements around the airfoil contour. The blade surface elements are refined by a factor of 10x near the leading edge (0-10% chord) and trailing edge (90-100% chord), compared to the elements along the remainder of the chord. A portion of the blade surface mesh is shown in Fig. 3a. The boundary layer in the wall normal direction is highly resolved, with the first element height set to ensure $y^+ < 1$, and at least 25 layers. A cross-sectional slice through the mesh in Fig. 3b shows the boundary layer elements around the airfoil. A refinement region, with element size prescribed as $1/2$ tip chord is established for the off-body area around the rotors, and extends $0.6R$ above the rotor plane, and $3R$ below (Figure 2b), with the mesh refinement below the rotor plane skewed towards the rear to better capture the rotor wakes as they convect downstream. The entire computational domain is comprised of 122 million elements, with 33 million in each rotating volume, and 56 million in the nonrotating volume. A mesh refinement study was performed in which the surface mesh size, edge refinement, boundary layer, and wake refinement were doubled independently. The results of the refinement study indicated that the thrust and torque changed by less than 1.5% and 2.5% respectively when compared to the original mesh (which is used for simulations in this study) (Ref. 18).

A detached eddy simulation (DES) is used with the Spalart-Allmaras (SA) turbulence model. All simulations are run initially using time steps corresponding to 10° of rotor rotation for several revolutions to reduce the computational cost of the rotor wake development. Each simulation is then continued for additional revolutions at 1° time steps until thrust and torque convergence is achieved. The initial 10° time steps

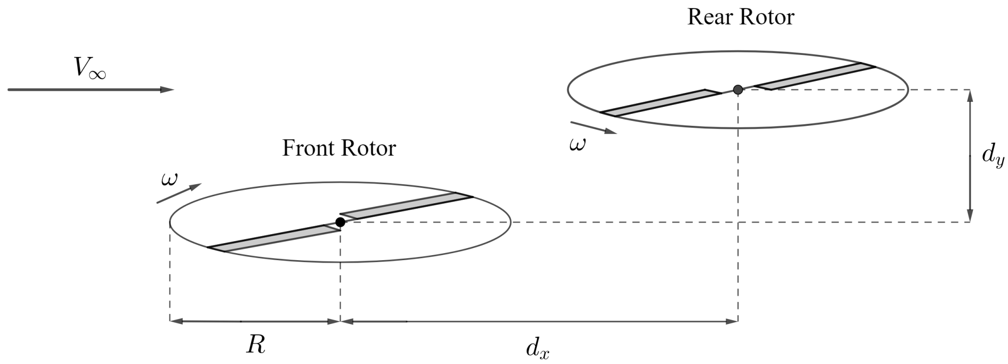

Figure 1: Longitudinal and vertical distance d_x and d_y

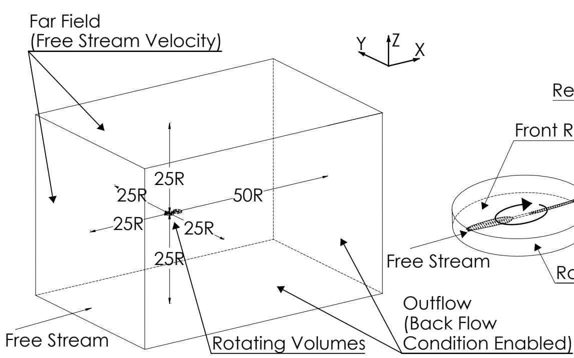

(a) Diagram of the computational domain

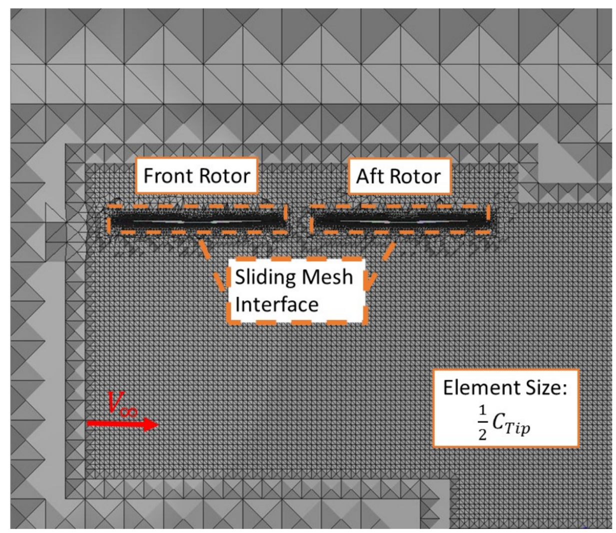

(b) Cross-section of wake mesh refinement

Figure 2: CFD simulation domain and mesh

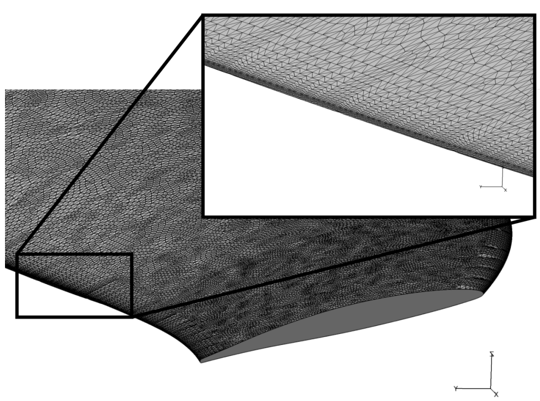

(a) Blade surface mesh near blade tip

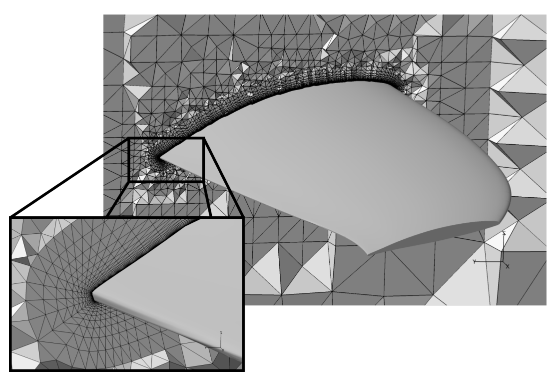

(b) Chordwise slice through the mesh

Figure 3: Mesh visualization

are possible without causing numerical divergence due to the stability afforded by the Streamline Upwind Petrov-Galerkin (SUPG) stabilized finite element method and Generalized-α implicit time integration method. The latter method was designed to suppress high frequency distrubances and allow solution stability with Courant-Friedrichs-Lewy number greater than 1 (Refs. 19,20). All runs were performed on 512 2.6 GHz Intel Xeon E5 -2650 processors, part of the Center for Computational Innovations at Rensselaer Polytechnic Institute.

Low-Fidelity Model – RMAC

The low-fidelity model used in this study is the Rensselaer Multicopter Analysis Code (RMAC, Ref. 21). Blade element theory is used to calculate the lift and drag at a differential blade element. In the RMAC simulations presented, each blade is divided into 48 radial segments, at which lift and drag are evaluated, resulting in a radial load distribution. Integration over the span and summing over the blades yields instantaneous loads (such as thrust and torque) at the rotor hub.

Rotor induced flow is modeled using a rigid, helical wake trailed from the blade tips (Ref. 22). The strength of each vortex filament is developed using a time-marching scheme, with 2° azimuthal resolution and a maximum wake age of 1440°. Utilizing the Biot-Savart law, the flow induced by the vortex filaments is evaluated at each radial station on both rotors, capturing the flow induced by each rotor on the other.

A helical vortex-wake model is applied (Ref. 22) to calculate the flow induced by the rotor. In this model, the rotor wake is represented by a vortex trailed from the tip of each rotors blade. As the rotor turns, the trailed vortex filaments are convected downward by the mean rotor induced flow and backward by the free-stream velocity. By using the Biot-Savart law, the vortex-induced flow can be calculated at any point in space, which makes it capable of predicting rotor-rotor interference effects. For the simulations presented, the maximum wake age is 4 rotor revolutions (1440°), with a 2° resolution, resulting in 180 distinct azimuthal locations for the rotor lift and drag distributions.

Multi-Fidelity Approach

For a fixed value of problem parameters, denoted by $\boldsymbol{\theta} = (d_x, d_y, V, DL)$, the low- and high-fidelity models can be used to compute the distributions of lift and drag over the front and aft rotors disks. These values are stored in a vector whose components are the value of lift/drag for the front/aft rotor at discrete radial and azimuthal coordinates. We denote the low-fidelity version of this vector (computed using RMAC) by $\boldsymbol{u}_i = \boldsymbol{u}(\boldsymbol{\theta}_i)$, and the high-fidelity counterpart (computed using CFD) by $\boldsymbol{v}_i = \boldsymbol{v}(\boldsymbol{\theta}_i)$. We will fuse these to generate a multi-fidelity vector, which we will denote by $\bar{\boldsymbol{v}}_i = \bar{\boldsymbol{v}}(\boldsymbol{\theta}_i)$. The construction of the multi-fidelity model is done in three different steps. The first involves solving a subset selection problem, which will lead to a surrogate model for the low-fidelity model. Finally, a lifting procedure is used to achieve the final expression of the multi-fidelity model.

Subset Selection Problem We consider a large set of points in the parameter space, $S = \{\boldsymbol{\theta}_i\}$, $i = 1,\ldots,N$, and compute the corresponding snapshots with the low-fidelity model $\boldsymbol{u}_i$. Out of these, we select the $n \ll N$ most significant ones. This means finding the snapshots to construct the n-dimensional subspace that can represent the set of the N snapshots with minimal l_2 error. The solution of this problem is found through a truncated rank revealing QR decomposition (Refs. 3, 10) of the snapshot matrix $\boldsymbol{U} = [\boldsymbol{u}_1, \ldots, \boldsymbol{u}_N]$,

$$\boldsymbol{U}\boldsymbol{P} = \boldsymbol{Q}\boldsymbol{R}. \tag{1}$$

In the equation above $\boldsymbol{Q}$ is an orthogonal matrix, $\boldsymbol{R}$ is a an upper-triangular matrix, and $\boldsymbol{P}$ is the permutation matrix. This matrix orders the snapshots from the most important to the least, such that the n snapshots we are interested are the first n columns of matrix $\boldsymbol{U}\boldsymbol{P}$.

We re-index the set $S = \{\boldsymbol{\theta}_i\}$ and the snapshots $\boldsymbol{u}_i$, $i = 1,\ldots,N$, to reflect this new ordering. The "important" parameter values can be included in the set $\bar{S} = \{\boldsymbol{\theta}_i\}_{i=1}^n$ and the important snapshots stored in the matrix

$$\bar{\boldsymbol{U}} = [\boldsymbol{u}_1, \ldots, \boldsymbol{u}_n]. \tag{2}$$

Low-rank Surrogate Model We can construct a low-fidelity surrogate model $\bar{\boldsymbol{u}}(\boldsymbol{\theta})$ as an expansion in terms of the important snapshots,

$$\bar{\boldsymbol{u}}(\boldsymbol{\theta}) = \sum_{i=1}^{n} \boldsymbol{u}_i g_i(\boldsymbol{\theta}). \tag{3}$$

The value of the functions g_i at a given set of parameters $\boldsymbol{\theta}_j$ are found by minimizing the residual,

$$\mathscr{R} = |\bar{\boldsymbol{u}}(\boldsymbol{\theta}_j) - \boldsymbol{u}(\boldsymbol{\theta}_j)|^2 = |\sum_{i=1}^{n} \boldsymbol{u}_i g_i(\boldsymbol{\theta}_j) - \boldsymbol{u}_j|^2, \tag{4}$$

yielding the following solution

$$\boldsymbol{g}(\boldsymbol{\theta}_j) = [g_i(\boldsymbol{\theta}_j)]_{i=1}^n = \boldsymbol{G}^{-1}\boldsymbol{f}_j \tag{5}$$

where $\boldsymbol{G} \equiv \bar{\boldsymbol{U}}^T\bar{\boldsymbol{U}} \in \mathbb{R}^{n\times n}$ is the Gramian matrix and $\boldsymbol{f}_j \equiv \bar{\boldsymbol{U}}^T\boldsymbol{u}_j \in \mathbb{R}^n$.

Lifting Procedure In the lifting step, we perform high-fidelity simulations at the important parameter values, $\bar{S} = \{\boldsymbol{\theta}_i\}_{i=1}^n$. This gives us the snapshots $\boldsymbol{v}_i, i = 1,\ldots,n$. We use these snapshots to replace the low-fidelity basis in Eq. 3, thereby "lifting" the low-fidelity surrogate model. This leads us to the final form of the multi-fidelity model

$$\bar{\boldsymbol{v}}(\boldsymbol{\theta}_j) = \sum_{i=1}^{n} \boldsymbol{v}_i g_i(\boldsymbol{\theta}_j). \tag{6}$$

A few remarks are in order here. First, we note that multi-fidelity approach describe above is general and can be applied to any set of low- and high-fidelity models. Second, the low-rank surrogate model and the lifting steps of this approach can be applied independently of the subset selection problem.

In particular, if a small number of high-fidelity snapshots are available a-priori, then one can forgo the portion of multi-fidelity approach dedicated to finding the important parameter values, and still apply the rest of the approach (low-rank approximation and lifting) to generate a multi-fidelity model. In the Numerical Results section described next, we consider this scenario.

NUMERICAL RESULTS

For the numerical application of the method, only the lifting procedure is used, as a set of CFD data, generated in Ref. 18, was available for use. Therefore, the low-fidelity snapshots employed as basis in Eq. 3 are the ones for which a high-fidelity counterpart is available. From here, the functions of the parameters $g_i(\boldsymbol{\theta})$ are computed as described in Eq. 5, and finally, a multi-fidelity model (Eq. 6) is created.

In the present study, the lift and drag analysis are kept distinct and are carried out separately. That is, a separate multifidelity model is created for lift and drag. In both cases, the components of the snapshot vector $\boldsymbol{u}_i$ are the value of lift/drag for the front and aft rotors at distinct radial and azimuthal coordinates.

The multi-rotor assembly considered in this study has two identical counter-rotating rotors aligned with the longitudinal axis, as shown in Fig. 1, where the front rotor rotates clockwise and the rear rotor rotates counter-clockwise. The rotors have a radius of $R = 0.8425\,\mathrm{m}$ (33.17 in) and the blades, whose planform is shown in Fig. 4, have a root pitch of 24° and linear twist rate of -12°.

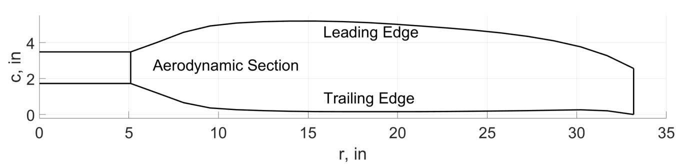

Figure 4: Blade planform for the rotors, reproduced from (Ref. 18).

The range of parameters for the design configurations and operational conditions are $d_x \in [2.25R, 4R]$, $d_y \in [0, 0.75R]$, $V \in [20, 70]$ kts and $DL \in [6, 12]\,\mathrm{lb\,ft^{-2}}$. In this 4-dimensional parameter space, we have the access to 248 low-fidelity RMAC simulations and 14 high-fidelity CFD simulations. Among the 14 CFD snapshots, only $n = 10$ are selected as the basis to "lift" the model, while the remainder are used to validate the multi-fidelity results. A summary of all the simulations available, represented as points in the parameter space, is presented in Fig. 5.

To ensure that the physics embedded in the whole set of low-fidelity snapshots is well captured and represented by this subset of 10, we can plot the contour of the relative l_2 error defined as:

$$e_i = \frac{||\boldsymbol{u}_i - \bar{\boldsymbol{u}}_i||}{||\boldsymbol{u}_i||} \times 100 \tag{7}$$

This quantity represents the difference between the surrogate model constructed from the subset of 10 low-fidelity snapshots as basis (Eq. 3), and the low-fidelity model itself. The distribution of this error in the parameter space is shown in Figs. 6 and 7. The error in the (d_x, d_y) plane is below 2% for both lift and drag distributions, and in the (V, DL) plane is below 10% for the lift and around $15-18\%$ for drag. We conclude that the subset of 10 snapshots used as basis is able to represent lift distribution with sufficient accuracy. To achieve better accuracy we would need more than 10 snapshots.

Once the surrogate model is created, we can apply the lifting procedure by replacing the low-fidelity snapshots with their high-fidelity counterparts, leading to the multi-fidelity model described in Eq. 6.

To validate the model, we compare its predictions with the high-fidelity CFD results at the four validation points in parameter space. In Fig. 10a, the lift distribution obtained with the CFD, RMAC and multi-fidelity models at validation point 1 (as defined in Fig. 5) are shown. To better visualize the error in the predicted lift distribution, the difference of the RMAC and multi-fidelity disk plots with respect to the benchmark CFD is also presented in Fig. 10b. In Fig. 11 the same is shown for the drag disk plots. Similarly, in Figs. 12 and 13 results are presented for validation point 4.

We observe that when compared with the CFD result, the RMAC model correctly identifies the regions of high and low lift/drag, but it over-predicts their maximum values for both front and rear rotors. The multi-fidelity model is able to correct that, as its predictions are closer to that of the high-fidelity CFD model. The quantitative performance of the models are presented in Tables 1 and 2, where we report the relative l_2 error

$$E_i = \frac{||\boldsymbol{v}_i - \bar{\boldsymbol{v}}_i||}{||\boldsymbol{v}_i||} \times 100 \tag{8}$$

in the predicted lift and drag distributions for the 4 validation points. We observe that the error for the multi-fidelity model is consistently smaller than that for the low-fidelity model.

The validated multi-fidelity model is used to generate integrated quantities of interest, in particular the front and aft rotor thrust, which is computed from the lift distribution at different rotor separation and operating conditions.

In Figs. 8 and 9, we show the forward and aft rotor thrust as a function of the longitudinal separation d_x and forward speed V, respectively. Prediction from the low-fidelity (RMAC) and multi-fidelity models, as well as the high-fidelity CFD model (wherever available) are shown.

As the longitudinal separation d_x is increased (keeping d_y and V fixed), the front rotor thrust remains relatively constant, regardless of nominal disk loading. As the front rotor is upstream of the aft rotor, it does not encounter significant interactional aerodynamic effects from the aft rotor. Thus, its thrust is independent of the aft rotor position, a behavior predicted by both the low-fidelity and multi-fidelity models.

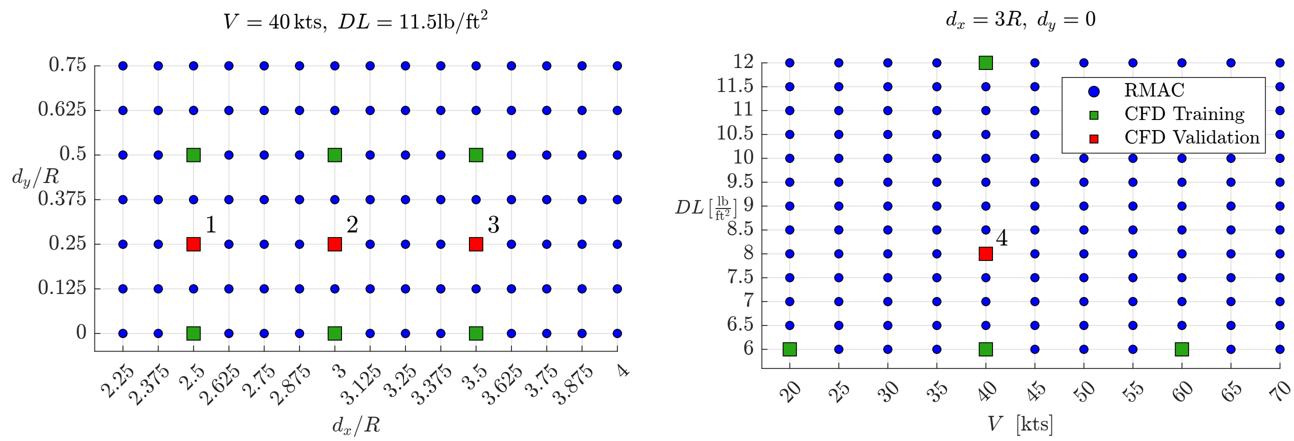

Figure 5: Snapshots available in the (d_x, d_y) plane corresponding to $V = 40$kts, $DL = 11.5\mathrm{lb\,ft}^{-2}$ and in the (V, DL) plane corresponding to $d_x = 3R,\ d_y = 0$.

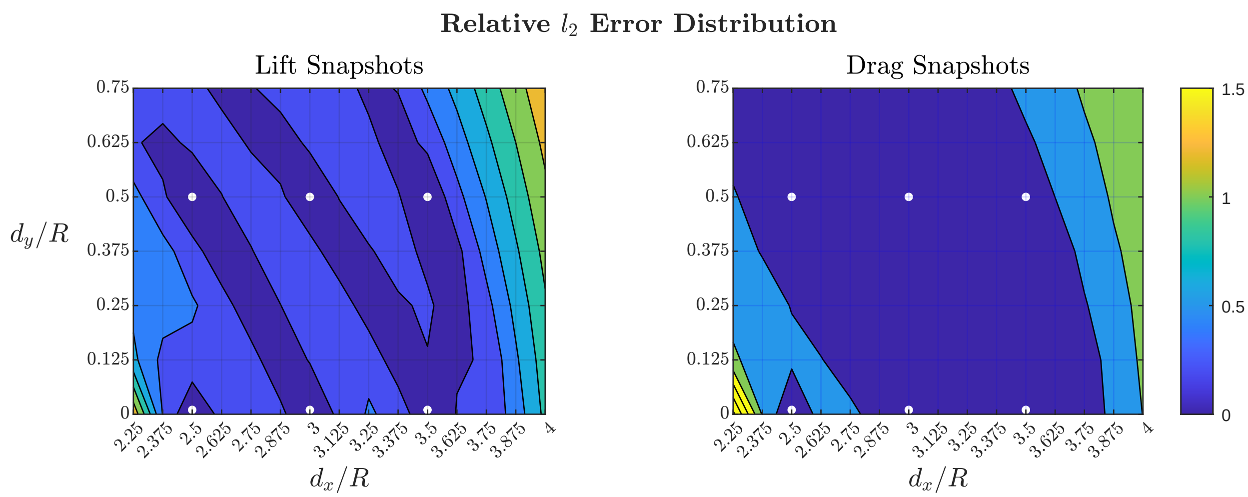

Figure 6: Relative error of the surrogate model with respect to the low-fidelity model

On the other hand, the aft rotor operates in close proximity to the front rotor's wake, so there is a strong interactional aerodynamic effect. Front-rotor-induced downwash on the aft rotor results in a relative lift deficit (Ref. 18), especially on the front half of the rotor. From a blade element perspective, extra downwash increases the induced inflow angle, reducing the local angle of attack, thereby reducing lift. Both models predict that as rotors are brought longitudinally closer together (smaller d_x), aft rotor thrust production diminishes, though this effect is more pronounced in the RMAC model. The closer the aft rotor is positioned relative to the front rotor, the closer it is to the front rotor wake, and the stronger the front-rotor-induced downwash. At both disk loadings however, the low-fidelity model predicts a stronger correlation between longitudinal separation and aft rotor thrust than the multi-fidelity model. Whereas RMAC predicts thrust to improve as separation is increased past 3.5R (and is approximately the same as the front rotor at $d_x = 4R$), the multi-fidelity surrogate does not predict any additional benefit past about 3R separation. Though it makes intuitive sense for the aft rotor thrust to approach the front rotor's thrust as the separation increases, the sensitivity of aft rotor thrust to its position is very low as predicted by CFD (as evidenced by the three validation points in Fig. 9), at least for that particular speed and rotor separation, though additional CFD data at $d_x = 0$ is needed to determine which trend is correct.

As speed increases, both RMAC and the multi-fidelity model predict greater thrust from both the front and rear rotors. Physically, the additional mass flux reduces the induced inflow, increasing the angle of attack of the fixed-pitch rotor blades, leading to higher lift.

CONCLUSIONS

In this paper we describe a method to combine two distinct models of different accuracy and cost, and generate a multi-fidelity model. This approach leverages results from a low-fidelity, low-cost model to span a parameter space, and uses a few selected a high-fidelity, high-cost model simulations to improve the accuracy. We applied this method to predicting

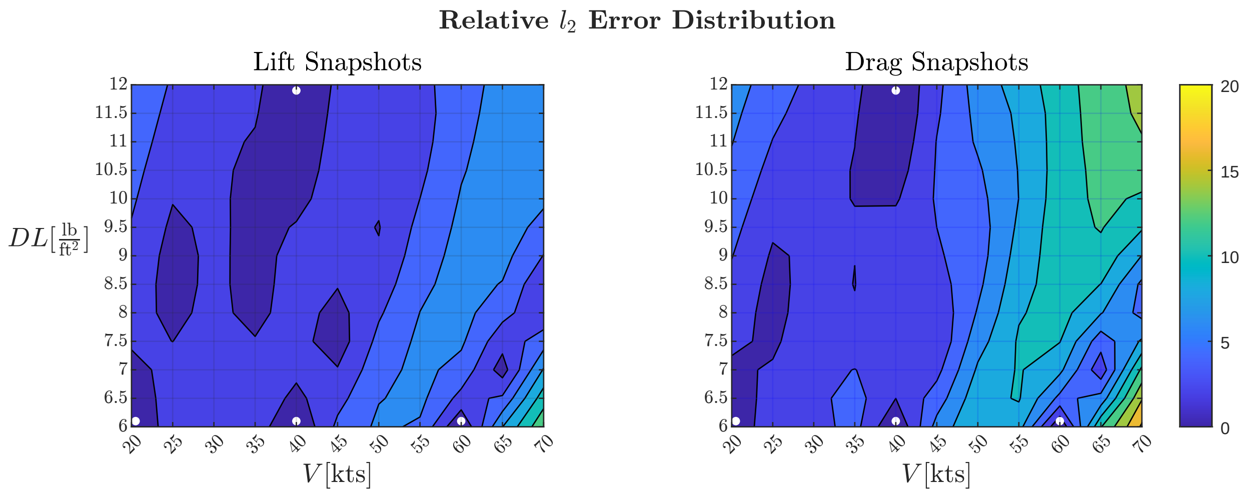

Figure 7: Relative error of the surrogate model with respect to the low-fidelity model

Table 1: Relative l_2 norm error in the low- and multi-fidelity (MF) models for lift distributions.

Lift	Validation 1		Validation 2		Validation 3		Validation 4	
	Front	Rear	Front	Rear	Front	Rear	Front	Rear
RMAC	41.60	43.79	42.95	43.31	42.64	42.91	39.37	41.55
MF	3.77	4.26	3.77	3.35	2.13	1.83	6.15	5.22

the rotor lift and drag distributions for a multicopter in forward flight. The low-fidelity model is based on the blade-element theory while the high-fidelity model is based on CFD. We have validated the performance of the multi-fidelity model with CFD data and quantified the gain in accuracy it engenders. We have also used it to examine the variation of thrust generated by the front and aft rotors as a function of longitudinal rotor separation and forward speed. Future work along this direction involves using the multi-fidelity approach to decide which high-fidelity simulation to perform, a more through exploration of quantities of interest like thrust, torque and power within the parametric space, and the use of other combination of low- and high-fidelity models.

ACKNOWLEDGMENTS

This work is carried out at the Rensselaer Polytechnic Institute under the Army/Navy/NASA Vertical Lift Research Center of Excellence (VLRCOE) Program, grant number W911W61120012, with Dr. Mahendra Bhagwat as Technical Monitor.

REFERENCES

1. Giselle Fernández-Godino, M., Park, C., Kim, N. H., and Haftka, R. T., "Issues in Deciding Whether to Use Multifidelity Surrogates," *AIAA Journal*, Vol. 57, (5), May 2019, pp. 2039–2054. DOI: 10.2514/1.j057750

2. Peherstorfer, B., Willcox, K., and Gunzburger, M., "Optimal Model Management for Multifidelity Monte Carlo Estimation," *SIAM Journal on Scientific Computing*, Vol. 38, (5), 2016, pp. A3163–A3194. DOI: 10.1137/15M1046472

3. Narayan, A., Gittelson, C., and Xiu, D., "A stochastic collocation algorithm with multifidelity models," *SIAM Journal of Computing*, Vol. 51, 2014, pp. 2005–2035.

4. Zhu, X., Narayan, A., and Xiu, D., "Computational Aspects of Stochastic Collocation with Multifidelity Models," *SIAM/ASA Journal on Uncertainty Quantification*, Vol. 2, 2014, pp. 444–463.

5. Hampton, J., Fairbanks, H. R., Narayan, A., and Doostan, A., "Practical error bounds for a non-intrusive bi-fidelity approach to parametric/stochastic model reduction," *Journal of Computational Physics*, Vol. 368, 2018, pp. 315–332.

6. Keshavarzzadeh, V., Kirby, R. M., and Narayan, A., "Parametric topology optimization with multiresolution finite element models," *International Journal for Numerical Methods in Engineering*, Vol. 119, 2019, pp. 567–589. DOI: 10.1002/nme.6063

7. Perry, D. J., Kirby, R. M., Narayan, A., and Whitaker, R. T., "Allocation strategies for high fidelity models in the multifidelity regime," *SIAM/ASA Journal on Uncertainty Quantification*, Vol. 7, 2019, pp. 203–231.

8. Papailiopoulos, D., Kyrillidis, A., and Boutsidis, C., "Provable deterministic leverage score sampling," *Proceedings of the 20th ACM SIGKDD international conference on Knowledge discovery and data mining*, 2014, pp. 997–1006.

Table 2: Relative l_2 norm error in low- and multi-fidelity (MF) models for drag distributions.

Drag	Validation 1		Validation 2		Validation 3		Validation 4	
	Front	Rear	Front	Rear	Front	Rear	Front	Rear
RMAC	59.25	55.31	59.30	56.23	58.76	56.47	57.81	52.30
MF	11.31	3.20	5.96	2.65	5.64	1.86	6.94	5.86

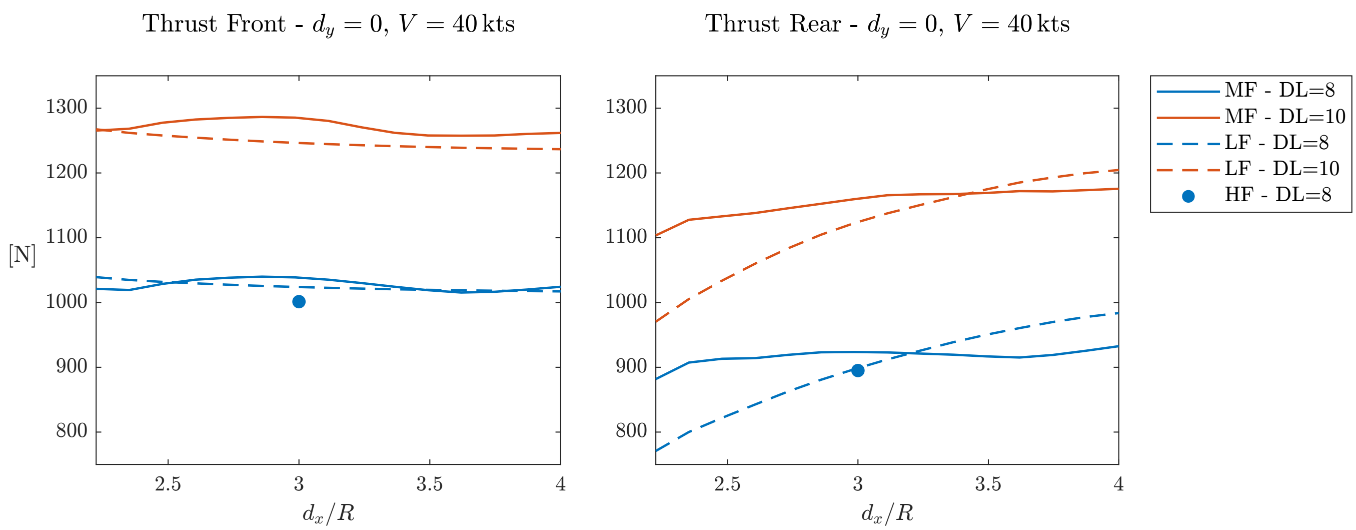

Figure 8: Thrust versus longitudinal separation for $d_y = 0$, $V = 40$kts.

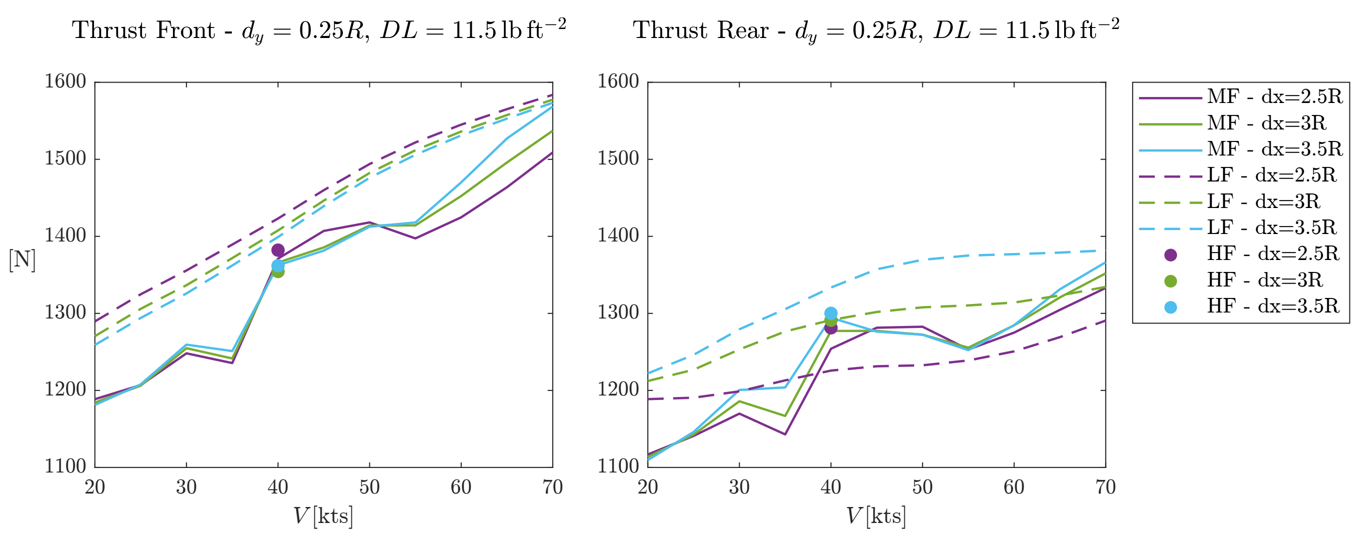

Figure 9: Thrust versus velocity for $d_y = 0.25R$, $DL = 11.5\text{lb-ft}^{-2}$.

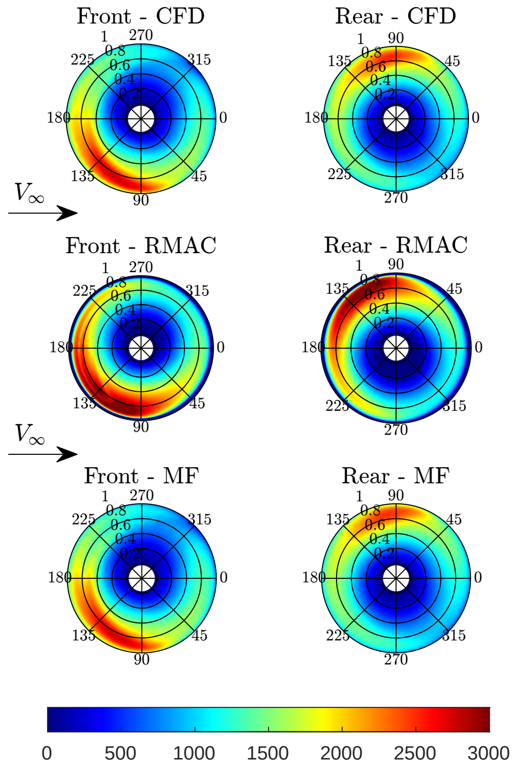

(a) Lift disk plots.

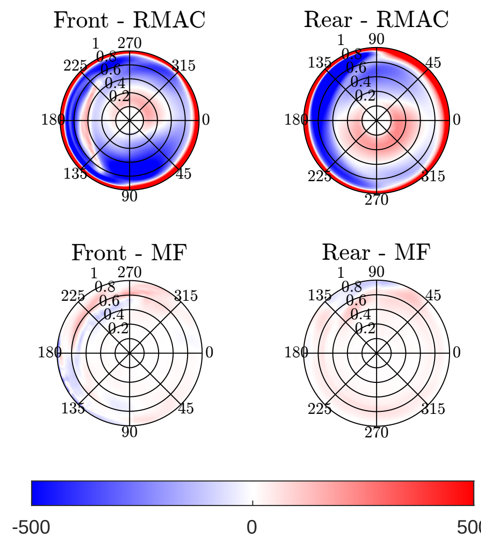

(b) Error in the Low- and Multi-Fidelity lift disk plots.

Figure 10: Validation Point 1: Low- and Multi-Fidelity lift disk plots (Units N/m).

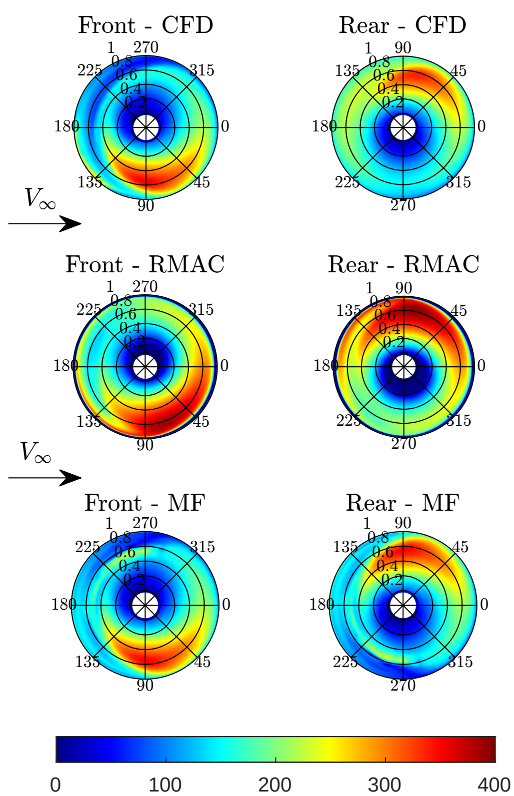

(a) Drag disk plots.

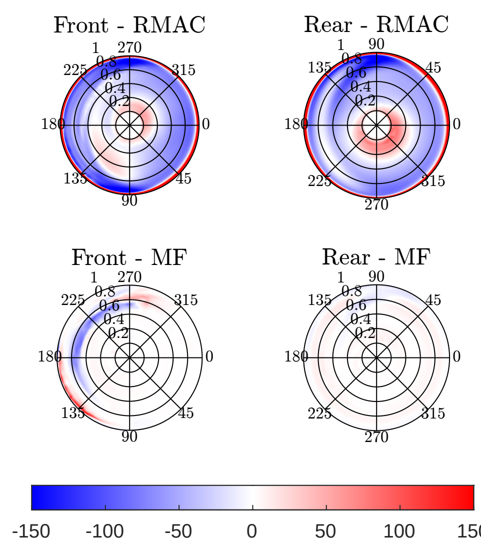

(b) Error in the Low- and Multi-Fidelity drag disk plots.

Figure 11: Validation Point 1: Low- and Multi-Fidelity drag disk plots (Units N/m).

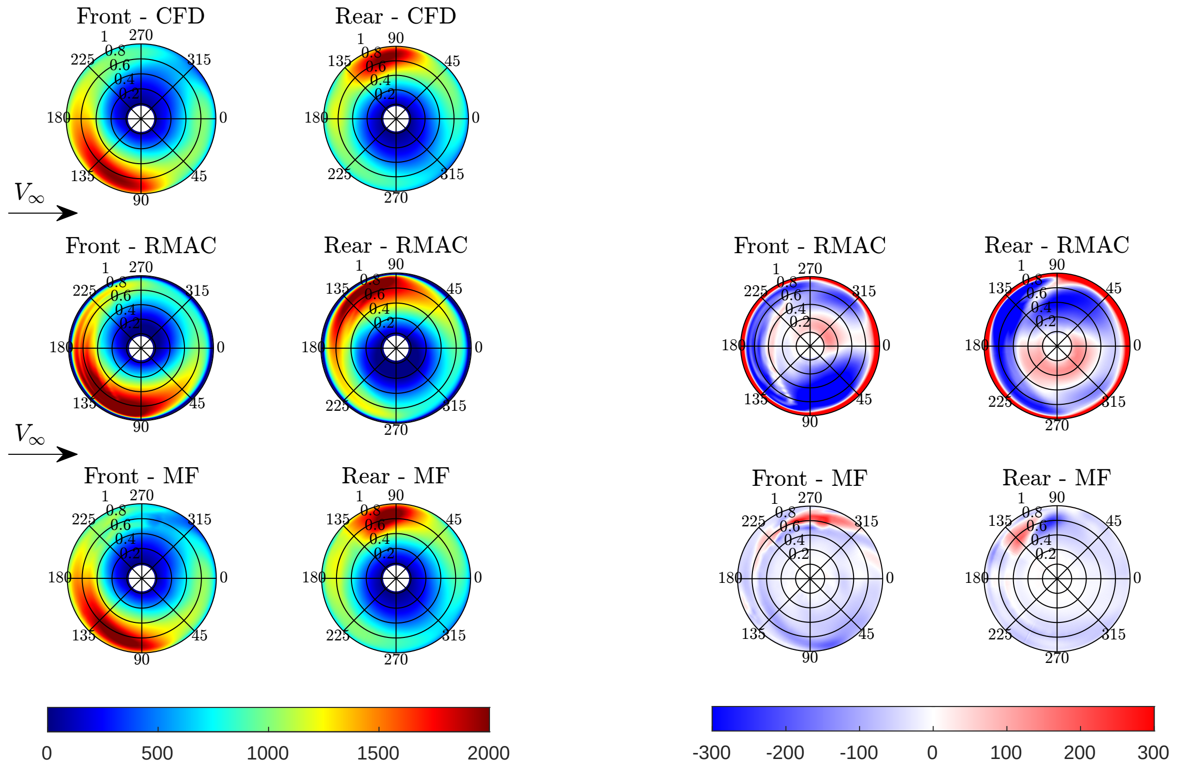

(a) Lift disk plots.

(b) Error in the Low- and Multi-Fidelity lift disk plots.

Figure 12: Validation Point 4: Low- and Multi-Fidelity lift disk plots (Units N/m).

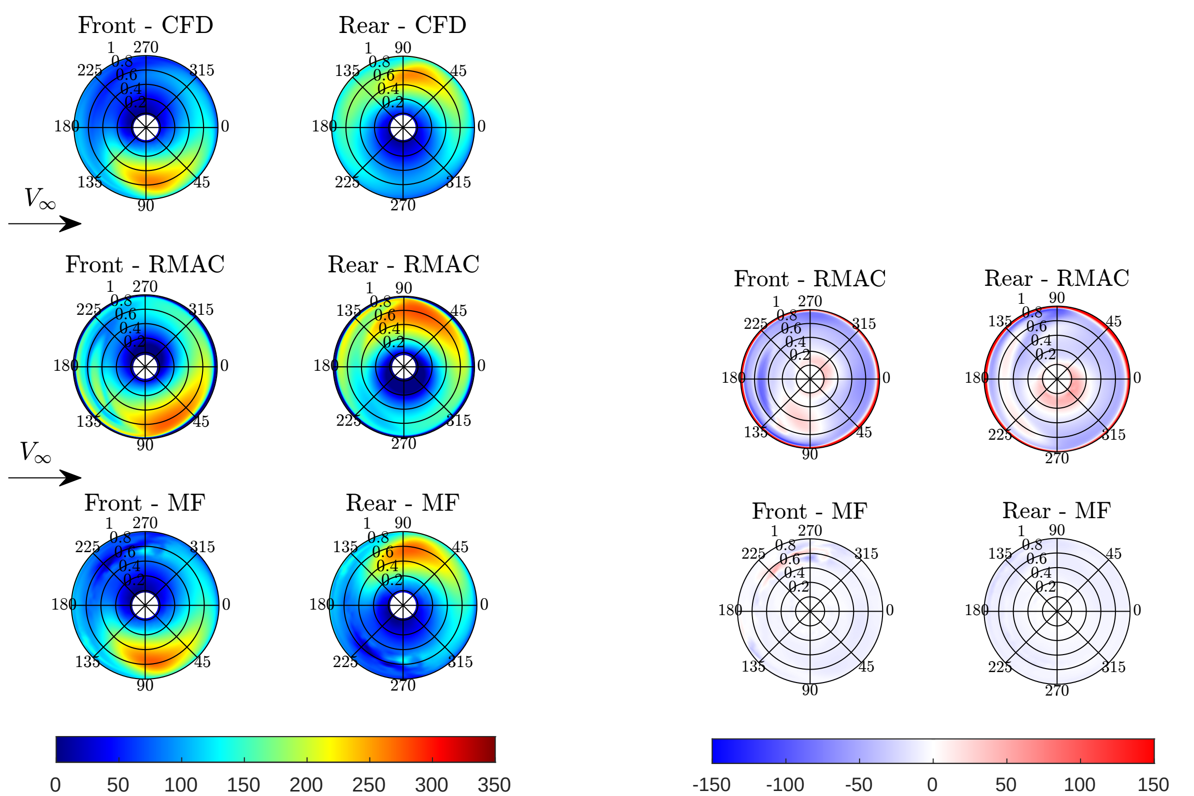

(a) Drag disk plots.

(b) Error in the Low- and Multi-Fidelity drag disk plots.

Figure 13: Validation Point 4: Low- and Multi-Fidelity drag disk plots (Units N/m).

9. Boutsidis, C., Drineas, P., and Magdon-Ismail, M., “Near-optimal column-based matrix reconstruction,” *SIAM Journal on Computing*, Vol. 10598, 2014, pp. 1–27.

10. Chan, T. F., “Rank Revealing QR Factorization,” *Linear Algebra Appl.*, Vol. 88/89, 1987, pp. 67–82.

11. Chan, T. F., and Hansen, P. C., “Some applications of the rank revealing QR factorization,” *SIAM Journal on Scientific Computing*, Vol. 13, 1992, pp. 727–741.

12. Gu, M., and Eisenstat, S. C., “Efficient Algorithms for Computing a Strong Rank-Revealing QR Factorization,” *SIAM Journal on Scientific Computing*, Vol. 17, 1996, pp. 848–869.

13. Chan, T. F., “Alternative to the SVD: Rank Revealing QR-Factorization,” *SPIE Proceedings*, Vol. 0696, 1986.

14. Hong, Y. P., and Pan, C. T., “Rank-Revealing QR Factorizations and the Singular Value Decomposition,” *Mathematics of Computation*, Vol. 58, (197), 1992, pp. 213–232.

15. Niemiec, R., and Gandhi, F., “Development and Validation of the Rensselaer Multicopter Analysis Code (RMAC): A Physics-Based Comprehensive Modeling Tool,” *75th Annual Forum of the American Helicopter Society*, 2019.

16. Pinti, O., Oberai, A., Healy, R., Niemiec, R., and Gandhi, F., “A Multi-Fidelity Approach to Predicting Interactional Aerodynamics,” *AIAA AVIATION FORUM*, 2020. DOI: 10.2514/6.2020-2796

17. Misiorowski, M., Gandhi, F., and Oberai, A. A., “Computational Study on Rotor Interactional Effects for a Quadcopter in Edgewise Flight,” *AIAA Journal*, Vol. 57, (12), 2019, pp. 5309–5319. DOI: 10.2514/1.J058369

18. Healy, R., Misiorowski, M., and Gandhi, F., “A Systematic CFD-Based Examination of Rotor-Rotor Separation Effects on Interactional Aerodynamics for Large eVTOL Aircraft,” *Proceedings of the 75th Annual Forum, (Philadelphia), VFS International*, 2019.

19. Jansen, K. E., Whiting, C. H., and Hulbert, G. M., “A generalized-alpha method for integrating the filtered Navier–Stokes equations with a stabilized finite element method,” *Computer Methods in Applied Mechanics and Engineering*, Vol. 190, 2000, pp. 305–319.

20. Brooks, A. N., and Hughes, T. J. R., “Streamline Upwind/Petrov-Galerkin Formulations for Convection Dominated Flows with Particular Emphasis on the Incompressible Navier-Stokes Equations,” *Computer Methods in Applied Mechanics and Engineering*, Vol. 32, 1982, pp. 199–259. DOI: 10.1002/nme.6063

21. Niemiec, R., *Development and Application of a Medium-Fidelity Analysis Code for Multicopter Aerodynamics and Flight Mechanics*, Ph.D. thesis, Rensselaer Polytechnic Institute, August 2018.

22. Leishman, J. G., “Rotor Wakes and Tip Vortices,” *Principles of Helicopter Aerodynamics, 2nd ed., Cambridge University Press, New York*, Vol. 32, 2006, pp. 567—654.